Isogeometric Kirchhoff-Love shell formulation for elasto-plasticity

Marreddy Ambati[a] · Josef Kiendl[b] · Laura De Lorenzis[a]

[a] Institute of Applied Mechanics
Technische Universität Braunschweig, Germany
[b] Department of Marine Technology
Norwegian University of Science and Technology, Trondheim, Norway

Abstract

An isogeometric thin shell formulation allowing for large-strain plastic deformation is presented. A stress-based approach is adopted, which means that the constitutive equations are evaluated at different integration points through the thickness, allowing the use of general 3D material models. The plane stress constraint is satisfied by iteratively updating the thickness stretch at the integration points. The deformation of the shell structure is completely described by the deformation of its midsurface, and, furthermore, the formulation is rotation-free, which means that the discrete shell model involves only three degrees of freedom. Several numerical benchmark examples, with comparison to fully 3D solid simulations, confirm the accuracy and efficiency of the proposed formulation.

Keywords: Isogeometric; Kirchhoff-Love; Thin shell; Finite strain; Elasto-plastic

1 Introduction

Shell structures play a central role in engineering design within many different disciplines, e.g., mechanical, aerospace, marine, and civil engineering, due to their high ratio of load capacity to self weight. In many cases, structural analysis of such structures needs to extend from the elastic to the plastic regime, e.g., when assessing the ultimate load capacity of the structure or when plastic deformations are part of the manufacturing process, like in sheet metal forming. The analysis of such highly nonlinear processes is widely done with nonlinear finite element (FE) analysis, and shell elements are typically employed for reducing the computational effort.

Formulating shell elements that account for large-strain plastic deformations is very challenging and a lot of research has been dedicated to such developments. From the modeling perspective, the crucial issue concerns the formulation and implementation of inelastic constitutive models. Two different classical approaches can be adopted: (i) to use *stress resultant* plasticity where the elasto-plastic constitutive models are formulated entirely based on stress resultants, see e.g. [1] - [6], or (ii) to define integration points in the thickness direction of the shell and to use *stress-based* three dimensional (3D) plasticity models. The stress resultants are obtained by integration through the thickness of the shell, see e.g. [7] - [11]. With the *stress resultant* formulation, the derivation of inelastic stress resultant constitutive models is very difficult from the solid constitutive models. Even the simplest von-Mises yield function leads to a rather complex functional form when expressed in stress resultants and also the

implementation of such constitutive models in the finite element framework is difficult, see the recent work by Dujc and Brank [6] and references therein. The *stress-based* formulation is widely used and is conceptually simple. It directly stems from the 3D theory, therefore solid constitutive models can be applied directly. For instance, this leads to the use of the standard return mapping algorithms for plasticity problems. This approach is adopted in this work.

In FE shell analysis, such an approach can be applied to thick shell formulations based on Reissner-Mindlin kinematics, which require only C^0 continuous discretization, or to thin shells models with the classical Kirchhoff-Love (KL) kinematics, for which a C^1 continuity is necessary. For a detailed review of shell theories and numerical formulations, see Bischoff et al. [12]. In the present work, the KL shell theory is considered. According to the KL shell hypothesis, the cross-sectional fibers in the undeformed configuration stay normal to the mid-plane and unstretched in the deformed configuration, which yields vanishing transverse shear deformations. The shell kinematics is thus described by the displacements of the middle surface and the thickness dimension is modeled by the surface normal vector, which is a function of the second derivatives of the displacements. This leads to the appearance of second derivatives in the equilibrium equation, which requires a C^1 continuous discretization of the displacements. It is well known that this requirement has been a major obstacle for the development of efficient KL FE shell formulations.

Isogeometric analysis (IGA) was introduced by Hughes and coworkers [13], with the main original purpose to bridge the gap between computer aided design and FE analysis. In IGA, higher-order and smooth basis functions, e.g., non-uniform rational B-splines (NURBS), are used to represent the geometry and to approximate the solution fields within the isoparametric approach. IGA has proven to provide remarkable advantages compared to the standard FE method based on conventional Lagrangian shape functions, mostly stemming from the higher and tailorable continuity of the basis functions. Over the last years, IGA has led to the new development of several efficient shell formulations, including rotation-free KL shells [14]-[19], Reissner-Mindlin shells [20]-[24], hierarchic shells [24]-[26] and solid shells [27]-[29]. The smoothness of the basis functions allows a straightforward implementation of C^1 thin shell models. An isogeometric formulation for geometrically nonlinear KL shells has been developed in [14] and its extension to the large strain regime in [15]. The developed formulation in [15] is such that an arbitrary 3D hyperelastic material model can be used for the shell analysis. The transverse normal strain is statically condensed using the plane stress condition (zero transverse normal stress). The main advantages of this approach are its simplicity and the possibility of its straightforward extension to any other complex constitutive law.

In this work, we extend the isogeometric shell model presented in [14, 15] to model elasto-plastic behaviour in KL shells at large deformations. A general *stress-based* 3D elasto-plastic constitutive model is used for the shell analysis. The classical J_2 plasticity with isotropic hardening based on the multiplicative decomposition of the deformation gradient in elastic and plastic parts [30, 31] is adopted. The backward Euler time integration scheme, required for the solution of the elasto-plastic constitutive equations, with the classical elastic predictor and plastic corrector (return-mapping) algorithm is used. The imposition of the plane stress condition is done at the integration points in a local iterative manner.

The paper is structured as follows. In Section 2, we provide the details of the proposed formulation. We first review the employed plasticity model in a solid mechanics setting, with the time integration algorithm of the elasto-plastic constitutive equations to be found in Appendix A. Then, we present the KL shell model, where the kinematics is described purely by the deformation of the middle surface, and we show how this can be extended to work with three-dimensional nonlinear constitutive models like the presented plasticity model. In Section 3, we illustrate the variational formulation. In Section 4, we present numerous benchmark examples and compare the solution of the proposed formulation with 3D solid element results and the available reference results from the literature. Section 5 closes the paper with some conclusions.

2 Formulation

In this section, the proposed formulation is presented in detail. We first review the employed plasticity model in a solid mechanics setting. Then, we present the KL shell model and extend it to work with three-dimensional nonlinear constitutive models like the presented plasticity model.

2.1 Finite strain plasticity

We assume a three-dimensional isochoric von-Mises (J_2) rate-independent plasticity theory in combination with isotropic hardening, and we adopt the framework based on the multiplicative decomposition of the deformation gradient in elastic and plastic parts and on maximum plastic dissipation developed by Simo [33], see also Simo and Hughes [30].
With the chosen approach, the deformation gradient, $\boldsymbol{F} = \mathrm{d}\boldsymbol{x}/\mathrm{d}\boldsymbol{X}$ ($\mathrm{d}\boldsymbol{x}, \mathrm{d}\boldsymbol{X}$ being infinitesimal line elements in the deformed and reference configurations), is decomposed in the product

$$\boldsymbol{F} = \boldsymbol{F}^{\mathrm{e}}\boldsymbol{F}^{\mathrm{p}}\,, \tag{1}$$

where $\boldsymbol{F}^{\mathrm{e}}$ and $\boldsymbol{F}^{\mathrm{p}}$ are, respectively, the elastic and plastic deformation gradients. This decomposition may be interpreted as a plastic deformation to a stress-free intermediate configuration, followed by a purely elastic deformation.
Based on the decomposition in eq. (1), the total and plastic right Cauchy-Green deformation tensors are given by

$$\boldsymbol{C} = \boldsymbol{F}^{\mathrm{T}}\boldsymbol{F}\,, \quad \boldsymbol{C}^{\mathrm{p}} = \boldsymbol{F}^{\mathrm{p}^{\mathrm{T}}}\boldsymbol{F}^{\mathrm{p}}\,, \tag{2}$$

and the elastic left Cauchy-Green deformation tensor is given by

$$\boldsymbol{b}^{\mathrm{e}} = \boldsymbol{F}^{\mathrm{e}}\boldsymbol{F}^{\mathrm{e}^{\mathrm{T}}}\,. \tag{3}$$

A useful relation between elastic and plastic deformation playing an important role for the elasto-plasticity theory employed is

$$\boldsymbol{b}^{\mathrm{e}} = \boldsymbol{F}\boldsymbol{C}^{\mathrm{p}^{-1}}\boldsymbol{F}^{\mathrm{T}}\,, \tag{4}$$

with its Lie derivative

$$\mathcal{L}\{\boldsymbol{b}^{\mathrm{e}}\} = \boldsymbol{F}\dot{\boldsymbol{C}}^{\mathrm{p}^{-1}}\boldsymbol{F}^{\mathrm{T}}\,. \tag{5}$$

The total (free) energy functional is expressed as the sum of elastic and plastic energy contributions as follows

$$\Phi(\boldsymbol{b}^{\mathrm{e}}, J^{\mathrm{e}}, \alpha) = \int_{\Omega_0} \left(\Psi^{\mathrm{e}}(\boldsymbol{b}^{\mathrm{e}}, J^{\mathrm{e}}) + \Psi^{\mathrm{p}}(\alpha)\right) dV \,, \tag{6}$$

where Ψ^{e} is the elastic strain energy density, $J^{\mathrm{e}} = \det[\boldsymbol{F}^{\mathrm{e}}]$, Ψ^{p} is the plastic energy density assuming isotropic hardening and α is the internal hardening variable.
For the purpose of describing the elastic response of the material, a neo-Hookean constitutive law of decoupled type is used, which will prove to be convenient for the subsequently introduced plasticity model. The elastic strain energy density Ψ^{e} is decomposed into a deviatoric (volume preserving) and volumetric (shape preserving) part

$$\Psi^{\mathrm{e}} = \Psi^{\mathrm{e}}_{\mathrm{vol}} + \Psi^{\mathrm{e}}_{\mathrm{dev}} \,, \tag{7}$$

with

$$\Psi^{\mathrm{e}}_{\mathrm{vol}} = \frac{\kappa_0}{2}\left(\frac{J^{\mathrm{e}^2}-1}{2} - \ln J^{\mathrm{e}}\right) \,, \quad \Psi^{\mathrm{e}}_{\mathrm{dev}} = \frac{\mu}{2}(\underline{I}^{\mathrm{e}}_b - 3) \,, \tag{8}$$

where $\underline{\boldsymbol{b}}^{\mathrm{e}} = J^{\mathrm{e}^{-2/3}}\boldsymbol{b}^{\mathrm{e}}$, $\underline{I}^{\mathrm{e}}_b = \mathrm{tr}[\underline{\boldsymbol{b}}^{\mathrm{e}}]$. Moreover, μ and κ_0 are the shear and the bulk modulus of the material, respectively. The Cauchy stress $\boldsymbol{\sigma}$ follows from the elastic strain energy density through the well-known relation (e.g. [37])

$$\begin{aligned}\boldsymbol{\sigma} &= \frac{2}{J}\boldsymbol{b}^{\mathrm{e}}\left(\frac{\partial \Psi^{\mathrm{e}}}{\partial \boldsymbol{b}^{\mathrm{e}}}\right) = \frac{2}{J}\boldsymbol{b}^{\mathrm{e}}\left(\frac{\partial \Psi^{\mathrm{e}}_{\mathrm{vol}}}{\partial \boldsymbol{b}^{\mathrm{e}}} + \frac{\partial \Psi^{\mathrm{e}}_{\mathrm{dev}}}{\partial \boldsymbol{b}^{\mathrm{e}}}\right) \\ &= \frac{1}{J}\left\{\frac{\kappa_0}{2}\left(J^2-1\right)\mathbf{I} + \mu \mathrm{dev}\{\underline{\boldsymbol{b}}^{\mathrm{e}}\}\right\} = \frac{1}{J}\left\{\boldsymbol{\tau}_{\mathrm{vol}} + \boldsymbol{\tau}_{\mathrm{dev}}\right\} \,,\end{aligned} \tag{9}$$

with $\boldsymbol{\tau}_{\mathrm{vol}}$ and $\boldsymbol{\tau}_{\mathrm{dev}}$ as the volumetric and deviatoric parts of the Kirchhoff stress tensor $\boldsymbol{\tau}$ and $\mathrm{dev}(\cdot) = (\cdot) - \frac{1}{3}\mathrm{tr}(\cdot)\mathbf{I}$. Taking into account that plastic deformation is stress-free and isochoric, the superscript e has been omitted in $\boldsymbol{\sigma}$ and J.
The von-Mises yield function is given by

$$f(\boldsymbol{\tau}_{\mathrm{dev}}, \alpha) = \|\boldsymbol{\tau}_{\mathrm{dev}}\| - \sqrt{\frac{2}{3}}R(\alpha) \leq 0 \,, \tag{10}$$

where $R(\alpha)$ is the hardening function. Suitable hardening functions for the materials considered in this work will be specified in the numerical examples in Section 4.
The associative flow rule stemming from the principle of maximum plastic dissipation can be shown to be [33]

$$\dot{\boldsymbol{C}}^{\mathrm{p}^{-1}} = -\frac{2}{3}\dot{\lambda} I^{\mathrm{e}}_b \boldsymbol{F}^{-1}\boldsymbol{n}\boldsymbol{F}^{-\mathrm{T}} \,, \quad \mathcal{L}\{\boldsymbol{b}^{\mathrm{e}}\} = -\frac{2}{3}\dot{\lambda} I^{\mathrm{e}}_b \boldsymbol{n} \,, \tag{11}$$

with $I^{\mathrm{e}}_b = \mathrm{tr}[\boldsymbol{b}^{\mathrm{e}}]$, $\boldsymbol{n} = \boldsymbol{\tau}_{\mathrm{dev}}/\|\boldsymbol{\tau}_{\mathrm{dev}}\|$ and $\dot{\lambda}$ as the plastic consistency factor. The evolution equation for the hardening variable is given by

$$\dot{\alpha} = \sqrt{\frac{2}{3}}\dot{\lambda} \,. \tag{12}$$

Loading and unloading conditions are governed by the Kuhn-Tucker relations

$$\dot{\lambda} \geq 0 \,, \quad f \leq 0 \,, \quad \dot{\lambda} f = 0 \,. \tag{13}$$

Solution of the elasto-plastic constitutive equations requires a time integration scheme, which is outlined in Appendix A.
For the shell model described in the next section, we express stresses by the second Piola-Kirchhoff stress tensor, which is obtained by the pull-back operation

$$\boldsymbol{S} = J\boldsymbol{F}^{-1}\boldsymbol{\sigma}\boldsymbol{F}^{-\mathrm{T}} . \tag{14}$$

Finally, the consistent material tangent $\mathbb{C}$ is obtained through the time integration scheme as given in the Appendix.

2.2 Kirchhoff-Love shell with finite strains

The KL shell model is based on the assumption that cross sections remain straight and stay normal to the middle surface during deformation, which means that transverse shear deformation is neglected. Accordingly, the description of the shell can be reduced to the description of its middle surface.
For the shell kinematics, we use the convective curvilinear coordinates θ^1, θ^2 of the midsurface, and θ^3 as the coordinate in thickness direction ($-0.5h \leq \theta^3 \leq 0.5h$ with h as the shell thickness). Furthermore, we employ index notation, where Greek indices take the values {1,2} and Latin indices take the values {1,2,3}, and summation over repeated indices is assumed.

Considering a point $\boldsymbol{x}_{\mathrm{m}}(\theta^1, \theta^2)$ on the middle surface, a local curvilinear basis is defined by the covariant base vectors $\boldsymbol{a}_\alpha$ and the unit normal vector $\boldsymbol{a}_3$

$$\boldsymbol{a}_\alpha = \frac{\partial \boldsymbol{x}_{\mathrm{m}}}{\partial \theta^\alpha} , \quad \boldsymbol{a}_3 = \frac{\boldsymbol{a}_1 \times \boldsymbol{a}_2}{|\boldsymbol{a}_1 \times \boldsymbol{a}_2|} , \tag{15}$$

see also Figure 1. With the above base vectors, the covariant metric and curvature coefficients of the surface are defined by the first and second fundamental forms of surfaces [32, 12]

$$a_{\alpha\beta} = \boldsymbol{a}_\alpha \cdot \boldsymbol{a}_\beta , \quad b_{\alpha\beta} = \boldsymbol{a}_{\alpha,\beta} \cdot \boldsymbol{a}_3 . \tag{16}$$

Due to the Kirchhoff hypothesis, the position vector of any point in the shell

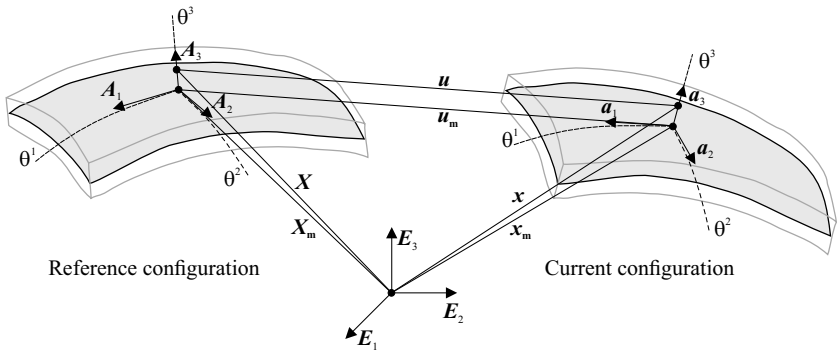

Figure 1: Schematic representation of a KL shell in the undeformed and deformed configurations.

continuum $\boldsymbol{x}$ can be described by the position vector of the corresponding point

on the midsurface and the normal vector as

$$\boldsymbol{x} = \boldsymbol{x}_{\mathrm{m}} + \theta^3 \boldsymbol{a}_3 \,. \tag{17}$$

The base vectors in the shell continuum are then obtained as [15]

$$\boldsymbol{g}_\alpha = \boldsymbol{a}_\alpha + \theta^3 \boldsymbol{a}_{3,\alpha} \,, \quad \boldsymbol{g}_3 = \boldsymbol{a}_3 \,, \tag{18}$$

and the corresponding metric coefficients are

$$g_{\alpha\beta} = a_{\alpha\beta} - 2\theta^3 b_{\alpha\beta}, \qquad g_{\alpha 3} = 0 \,, \quad g_{33} = a_{33} = 1 \,. \tag{19}$$

We note that the quadratic term $(\theta^3)^2$ in $g_{\alpha\beta}$ has been neglected corresponding to the classical assumption of a linear strain distribution through the thickness, while $g_{\alpha 3} = 0$ due to the Kirchhoff assumption.

Contravariant base vectors $\boldsymbol{g}^i$ are defined by $\boldsymbol{g}^i \cdot \boldsymbol{g}_j = \delta^i_j$, with δ^i_j as the Kronecker symbol. They can be computed as $\boldsymbol{g}^\alpha = g^{\alpha\beta}\boldsymbol{g}_\alpha$, $\boldsymbol{g}^3 = \boldsymbol{g}_3$, with $g^{\alpha\beta}$ as the contravariant metric coefficients, which can be obtained by matrix inversion $[g^{\alpha\beta}] = [g_{\alpha\beta}]^{-1}$. The contravariant metric coefficients are completed by $g^{\alpha 3} = g_{\alpha 3} = 0$ and $g^{33} = g_{33} = 1$.

Eqs. (15)–(19) have been written for the deformed configuration, indicated by lower case letters ($\boldsymbol{x}, \boldsymbol{a}_\alpha, a_{\alpha\beta}$, etc.), but they hold analogously for the initial configuration, which is indicated by upper case letters ($\boldsymbol{X}, \boldsymbol{A}_\alpha, A_{\alpha\beta}$, etc.). Note that these equations do not account for the thickness change in the deformed configuration, which will be corrected in the kinematic and constitutive equations as shown in the following.

Within a curvilinear frame formed by the contravariant basis of the undeformed configuration $\boldsymbol{G}^i \otimes \boldsymbol{G}^j$, the coefficients of the deformation gradient $\boldsymbol{F}$ and the right Cauchy-Green deformation tensor are generally given as

$$\begin{aligned} F_{ij} &= \boldsymbol{G}_i \cdot \boldsymbol{g}_j, \\ C_{ij} &= \boldsymbol{g}_i \cdot \boldsymbol{g}_j = g_{ij}. \end{aligned} \tag{20}$$

It is important to note that these general equations (20) have to be modified for shells in finite strains, in order to consider also the thickness deformation, which was neglected in the geometry definitions (17)-(19). Considering the thickness stretch λ_3, we have to correct the thickness base vector as

$$\boldsymbol{g}_3 = \lambda_3 \boldsymbol{a}_3. \tag{21}$$

Accordingly, the corrected deformation tensors are obtained as

$$\begin{aligned} F_{i\beta} = \boldsymbol{G}_i \cdot \boldsymbol{g}_\beta, \quad F_{i3} = \lambda_3 \boldsymbol{G}_i \cdot \boldsymbol{a}_3, \\ C_{\alpha\beta} = g_{\alpha\beta}, \quad C_{\alpha 3} = 0, \quad C_{33} = \lambda_3^2, \end{aligned} \tag{22}$$

The general problem is that the thickness deformation cannot be determined directly from the deformation, since the shell model describes only the deformation of the middle surface. However, it can be determined by using the plane stress condition $S^{33} = 0$ as an additional equation. In [15], such an approach was shown in the context of hyperelastic materials, where $S^{33} = 0$ was used to solve for the unknown component C_{33}. In the present paper, we adopt this approach and extend it to elasto-plastic materials, where we typically need to

work with the deformation gradient $\boldsymbol{F}$. As can be seen in (22), only one component of the Cauchy-Green deformation tensor, namely C_{33}, is affected by the thickness deformation, while for the deformation gradient the three components F_{13}, F_{23}, F_{33} are affected. However, they are all determined by the thickness stretch λ_3, which, in turn, can be obtained as the square root of C_{33}. Accordingly, we first solve for C_{33}, and then update also F_{i3}.

For the proposed approach we linearize the plane stress condition and solve it for C_{33}

$$S^{33} + \frac{\partial S^{33}}{\partial C_{33}} \Delta C_{33} = S^{33} + \frac{1}{2} \mathbb{C}^{3333} \Delta C_{33} = 0, \tag{23}$$

so

$$\Delta C_{33} = -2 \frac{S^{33}}{\mathbb{C}^{3333}}. \tag{24}$$

The correction term ΔC_{33} is used to iteratively update C_{33}, where a superscript I indicates the iteration step

$$C_{33}^{(I+1)} = C_{33}^{(I)} + \Delta C_{33}^{(I)}. \tag{25}$$

From the updated C_{33}, we compute the update of the thickness stretch

$$\lambda_3^{(I+1)} = \sqrt{C_{33}^{(I+1)}}, \tag{26}$$

which is finally used to compute the updated deformation gradient

$$\begin{aligned} F_{i\beta}^{(I+1)} &= F_{i\beta}^{(I)}, \\ F_{i3}^{(I+1)} &= \lambda_3^{(I+1)} \boldsymbol{G}_i \cdot \boldsymbol{a}_3. \end{aligned} \tag{27}$$

With the updated $\boldsymbol{F}$, the stress and material tangent tensors $\boldsymbol{S}$, $\mathbb{C}$ are recomputed according to the procedure outlined in Section 2.1 and the Appendix. This procedure (23)-(27) is repeated until the plane stress condition is satisfied within a specified tolerance.

As initial value for λ_3, we take the converged value from the previous time step, and $\lambda_3 = 1$ in the first time step. It should be noted that this iterative procedure is done locally at each integration point. Once it is converged, i.e., the correct $\boldsymbol{S}$, $\mathbb{C}$ have been obtained, only the in-plane stress components $S^{\alpha\beta}$ are considered for shell analysis. The energetically conjugate strains are the in-plane Green-Lagrange strains $E_{\alpha\beta}$, which are obtained as

$$\begin{aligned} E_{\alpha\beta} &= \varepsilon_{\alpha\beta} + \theta^3 \kappa_{\alpha\beta}, \\ \varepsilon_{\alpha\beta} &= \frac{1}{2}(a_{\alpha\beta} - A_{\alpha\beta}), \\ \kappa_{\alpha\beta} &= B_{\alpha\beta} - b_{\alpha\beta}, \end{aligned} \tag{28}$$

where $\varepsilon_{\alpha\beta}$ are the membrane strains and $\kappa_{\alpha\beta}$ the curvature changes, also called bending strains. The total differential of in-plane stress and strain components are related by

$$\mathrm{d}S^{\alpha\beta} = \hat{\mathbb{C}}^{\alpha\beta\gamma\delta} \, \mathrm{d}E_{\gamma\delta} \ . \tag{29}$$

where $\hat{\mathbb{C}}^{\alpha\beta\gamma\delta}$ is the statically condensed material tensor defined as

$$\hat{\mathbb{C}}^{\alpha\beta\gamma\delta} = \mathbb{C}^{\alpha\beta\gamma\delta} - \frac{\mathbb{C}^{\alpha\beta 33} \mathbb{C}^{33\gamma\delta}}{\mathbb{C}^{3333}} \ . \tag{30}$$

The stresses are integrated through the thickness and represented by membrane forces $\boldsymbol{N}$ and bending moments $\boldsymbol{M}$

$$\begin{aligned} \boldsymbol{N} &= \int_{-h/2}^{h/2} \boldsymbol{S}\, \mathrm{d}\theta^3\,, \\ \boldsymbol{M} &= \int_{-h/2}^{h/2} \boldsymbol{S}\, \theta^3\, \mathrm{d}\theta^3\,, \end{aligned} \tag{31}$$

and their total differentials are obtained as

$$\begin{aligned} \mathrm{d}\boldsymbol{N} &= \hat{\mathbb{C}}_A \mathrm{d}\boldsymbol{\varepsilon} + \hat{\mathbb{C}}_B \mathrm{d}\boldsymbol{\kappa}\,, \\ \mathrm{d}\boldsymbol{M} &= \hat{\mathbb{C}}_B \mathrm{d}\boldsymbol{\varepsilon} + \hat{\mathbb{C}}_D \mathrm{d}\boldsymbol{\kappa}\,. \end{aligned} \tag{32}$$

where $\hat{\mathbb{C}}_A, \hat{\mathbb{C}}_B, \hat{\mathbb{C}}_D$ are the thickness-integrated material tensors

$$\hat{\mathbb{C}}_A = \int_{-h/2}^{h/2} \hat{\mathbb{C}}\, \mathrm{d}\theta^3\,, \quad \hat{\mathbb{C}}_B = \int_{-h/2}^{h/2} \hat{\mathbb{C}}\, \theta^3\, \mathrm{d}\theta^3\,, \quad \hat{\mathbb{C}}_D = \int_{-h/2}^{h/2} \hat{\mathbb{C}}\, (\theta^3)^2\, \mathrm{d}\theta^3\,. \tag{33}$$

We note that in contrast to linear shell models, the thickness integrals in (31) and (33) cannot be computed analytically, but numerically [15].

With the approach outlined above, shell analysis can be performed with arbitrary three-dimensional material models, which might be based on the deformation tensor $\boldsymbol{C}$ as typical for hyperelastic models, or the deformation gradient $\boldsymbol{F}$ as typical for plasticity models. Since such materials models are mostly formulated in a Cartesian coordinate frame it is useful to define a local Cartesian basis aligned with the shell middle surface as follows

$$\bar{\boldsymbol{E}}_1 = \frac{\boldsymbol{G}_1}{\|\boldsymbol{G}_1\|}\,, \quad \bar{\boldsymbol{E}}_2 = \frac{\boldsymbol{G}_2 - (\boldsymbol{G}_2 \cdot \bar{\boldsymbol{E}}_1)\bar{\boldsymbol{E}}_1}{\left\|\boldsymbol{G}_2 - (\boldsymbol{G}_2 \cdot \bar{\boldsymbol{E}}_1)\bar{\boldsymbol{E}}_1\right\|}\,, \quad \bar{\boldsymbol{E}}_3 = \boldsymbol{G}_3\,. \tag{34}$$

The base vectors $\bar{\boldsymbol{E}}_i$ represent the local Cartesian basis, where the upper bar $\bar{(\cdot)}$ refers to their local nature. The coefficients of the deformation gradient in the local Cartesian system, $\bar{F}_{ij}$, are then obtained by

$$\begin{aligned} \bar{F}_{ij} &= F_{mn} \left(\bar{\boldsymbol{E}}_i \cdot \boldsymbol{G}^m\right) \left(\boldsymbol{G}^n \cdot \bar{\boldsymbol{E}}_j\right) \\ \boldsymbol{F} &= \bar{F}_{ij} \bar{\boldsymbol{E}}_i \otimes \bar{\boldsymbol{E}}_j\,. \end{aligned} \tag{35}$$

Similar transformations apply to the coefficients of the strain tensors. As a consequence, also the stress and material tensors will be expressed in the local Cartesian coordinate system.

3 Variational formulation

In this work, a conventional incremental FE procedure is adopted to solve the elasto-plastic boundary value problem, where the unknowns are the elastic strain, the hardening variable and the plastic multiplier. The plastic strain does not appear explicitly in the initial value problem [31, 30].
The FE formulation is based on the Principle of Virtual Work. The internal

and external virtual quantities for the KL shell take the following form [40]

$$\begin{aligned} \delta W_{\text{int}}^{\text{u}} &= \int_{\Omega_0} \delta \boldsymbol{E} : \boldsymbol{S} \, dV = \int_{A_0} (\delta \boldsymbol{\varepsilon} : \boldsymbol{N} + \delta \boldsymbol{\kappa} : \boldsymbol{M}) \, dA \,, \\ \delta W_{\text{ext}}^{\text{u}} &= \int_{A_0} \delta \boldsymbol{u} \cdot \boldsymbol{f} \, dA \,, \end{aligned} \tag{36}$$

where Ω_0 is the initial domain, A_0 denotes the undeformed midsurface, and $\boldsymbol{f}$ is the external load per unit area. Note that $\boldsymbol{E}$ is the tensorial form of E_{ab} defined in (28). Here the assumption that a differential volume element dV can be approximated by $dV \approx h \, dA$ applies.
In the FE procedure, with residual vector $\boldsymbol{R}^{\text{u}} = \boldsymbol{F}_{\text{ext}}^{\text{u}} - \boldsymbol{F}_{\text{int}}^{\text{u}}$, the vector of internal nodal forces $\boldsymbol{F}_{\text{int}}^{\text{u}}$ is obtained by performing the variation of $\delta W_{int}^{\text{u}}$ with respect to the discrete nodal displacement $\boldsymbol{u}$. Its components read

$$F_{\text{int}\,r}^{\text{u}} = \int_{A_0} \left(\frac{\partial \boldsymbol{\varepsilon}}{\partial u_r} : \boldsymbol{N} + \frac{\partial \boldsymbol{\kappa}}{\partial u_r} : \boldsymbol{M} \right) dA \,, \tag{37}$$

$\boldsymbol{F}_{\text{ext}}^{\text{u}}$ is the external load vector. The linearization of the residual vector yields the tangent stiffness matrix $\boldsymbol{K}^{\text{u}}$, which, for displacement-independent loads, is obtained from the linearization of the internal force vector. Its components are

$$K_{rs}^{\text{u}} = \int_{A_0} \left(\frac{\partial \boldsymbol{\varepsilon}}{\partial u_r} : \frac{\partial \boldsymbol{N}}{\partial u_s} + \frac{\partial^2 \boldsymbol{\varepsilon}}{\partial u_r \partial u_s} : \boldsymbol{N} + \frac{\partial \boldsymbol{\kappa}}{\partial u_r} : \frac{\partial \boldsymbol{M}}{\partial u_s} + \frac{\partial^2 \boldsymbol{\kappa}}{\partial u_r \partial u_s} : \boldsymbol{M} \right) dA \,. \tag{38}$$

The linearized equation system, which is solved for the incremental displacement vector $\Delta \tilde{\boldsymbol{u}}$, finally reads

$$\boldsymbol{K}^{\text{u}} \, \Delta \tilde{\boldsymbol{u}} = \boldsymbol{R}^{\text{u}}. \tag{39}$$

The detailed linearization of $\boldsymbol{\varepsilon}$ and $\boldsymbol{\kappa}$ with respect to u_r, u_s and further implementation aspects are presented in [15, 16].

4 Numerical tests

In this section, the capability of the proposed formulation to model the elasto-plastic behaviour in shells is illustrated by means of several numerical examples. In all tests, quadratic NURBS shape functions and three Gauss points for the thickness integration are used. All obtained results are compared to reference results, either from the literature, or from results of full 3D simulations with isogeometric solid elements. In the latter case, quadratic NURBS solid elements are used, with the same in-plane mesh as the shell model and with a single element in the thickness direction. All examples were computed with an in-house code on a series of meshes but in the following we present only those meshes with converged results.

4.1 Simply supported plate

Firstly, a simply supported plate under uniform pressure loading is studied. The geometry and boundary conditions of the problem are illustrated in Figure 2, whereas the material parameters are $E = 70 \times 10^3$ N/mm^2, $\nu = 0.32$ and

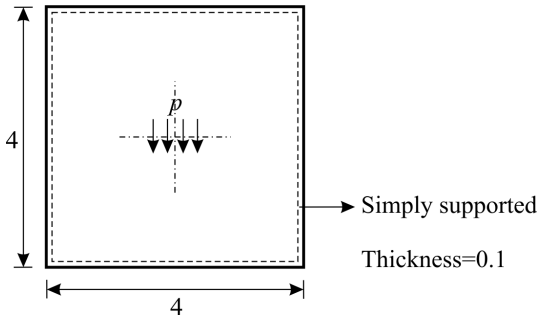

Figure 2: Simply supported plate. Geometry and boundary conditions. Dimensions in mm.

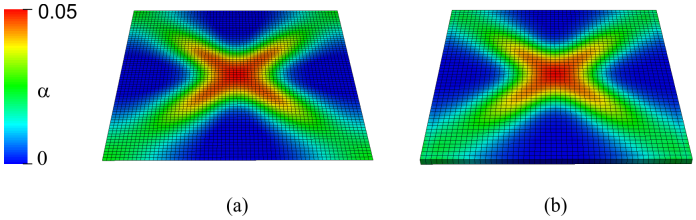

Figure 3: Simply supported plate. (a-b) Hardening variable for simply supported plate at U_{norm}=0.35 mm obtained with (a) KL shell and (b) solid elements.

$R(\alpha) = 243$ (perfect plasticity). Exploiting symmetry, only one quarter of the plate is modeled and discretized uniformly with 1024 elements. The simulation is performed under arc-length control. At every load increment, the norm of the total displacement vector, defined as $U_{norm} = \sqrt{\frac{U^T U}{n_{cp}}}$ is monitored, where U is the vector of the control point displacements and n_{cp} is the total number of control points. As mentioned already, the strategy to enforce plane stress condition can be adopted for any material model. In this example, a geometrically linear shell model combined with small-strain elasto-plasticity, isotropic hardening and additive decomposition of the total strain into elastic and plastic strain is used. For linear shell theory see [14] and for small-strain elasto-plasticity see [31].

The results for both the shell and solid computations are shown in Figure 3 in terms of contour plots of the hardening variable. For the shell, the hardening variable at Gauss point $(-\sqrt{\frac{3}{5}})$ in the thickness direction is displayed, projected onto the mid surface. As expected, the equivalent plastic strain is maximum in the plate center and branches form towards the plate corners. The pressure-displacement curves are given in Figure 4 along with analytic upper and lower bound limit load solutions, see e.g. [41]. A very good agreement between the shell and solid results can be observed. Furthermore, the curves clearly show that the numerical results lie within the analytical limit bounds. For the shells, although the required plane stress condition is enforced in local iterative man-

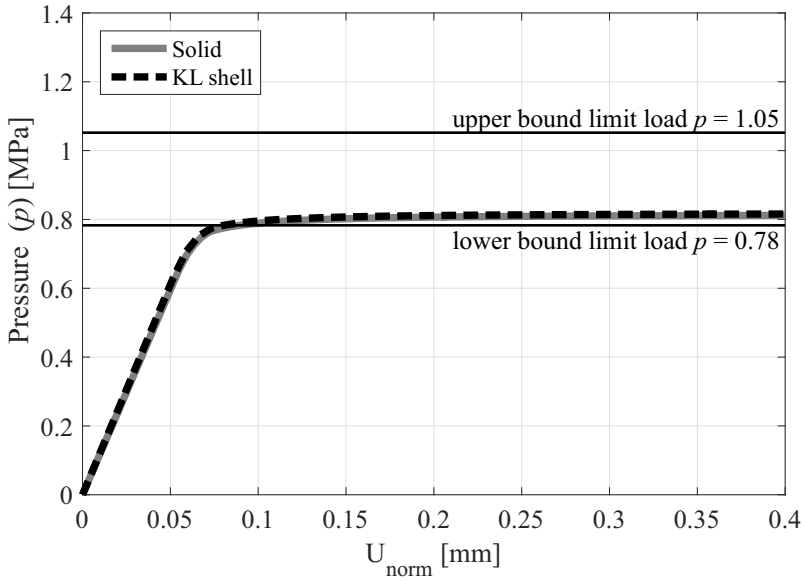

Figure 4: Simply supported plate. Pressure-norm of the total displacement curves. Comparison between KL shell and solid elements. Analytical limit load solutions [41].

ner, the computational cost is quite low compared to the solid computations because only the middle surface is modeled and there are only three degrees of freedom per control point.

4.2 Plane stress necking problems

A flat specimen and a hollow cylinder under tensile loading are studied, considering fully nonlinear elasto-plasticity as described in Section 2.1. The geometric properties and boundary conditions are shown in Figure 5, the material parameters are $E = 189 \times 10^3$ N/mm^2, $\nu = 0.29$, with a nonlinear hardening law $R(\alpha) = 343 + (680 - 343)\,(1 - \exp(-16.93\alpha)) + 300\alpha$ taken from [46]. A mesh with 1000 elements for the flat specimen and 4000 elements for the cylinder is used. The simulations are performed under displacement control with fixed displacement increments.

For the flat tensile specimen, Figure 6 (a-c) reports the evolution of the hardening variable on the deformed configuration at various loading stages obtained with KL shell elements. After the elastic state, from the yield point until the ultimate stress the material behaves plastically ($\alpha > 0$) with uniform deformations. As the deformation progresses, the hardening variable concentrates in the necking zone, taking the maximum value in the center of the specimen. The final result obtained with 3D solid elements can be seen in Figure 6 (d). The corresponding load-displacement curve is presented in Figure 7, where it can be observed that the KL shell results coincide with 3D solid solution. Note that the present formulation is based on local plasticity and it is well known that in the

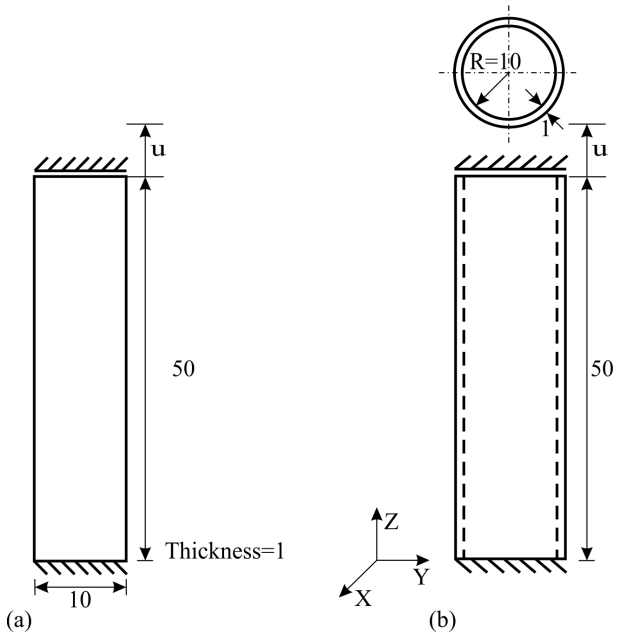

Figure 5: Plane stress necking problem. Geometry and boundary conditions. (a) flat tensile specimen (b) hollow cylinder. Dimensions in mm.

necking region, due to strong softening behaviour, the results may be sensitive to the mesh. A way to overcome this problem is to adopt gradient plasticity formulations [42]-[45].

For the hollow cylinder specimen, Figure 8 (a-c) shows the contour of the hardening variable at various loading stages on the deformed configuration obtained with KL shell elements. After the ultimate point, the hardening variable localizes in the central region of the specimen and has the maximum value along the entire circumference of the cylinder in the necking zone. Figure 8 (d) shows the final result obtained with the 3D solid element. The corresponding load-displacement curves from the numerical simulations are given in Figure 9, where we can see a perfect agreement of the proposed formulation with the 3D solution. As before, for both specimens, the shell elements require significantly lower computational time compared to the solid elements.

4.3 Pinched hemisphere at large elasto-plastic deformations

A full hemispherical shell is one of the standard benchmark problems in non-linear shell computations, see e.g [29, 2, 47, 52, 49, 6]. The geometry, loading conditions and FE mesh of the model are depicted in Figure 10. The material parameters are $E = 100$ N/mm^2, $\nu = 0.2$ and linear hardening law $R(\alpha) = 2 + 30\alpha$ taken from [47]. Due to symmetry, only one quarter of the shell is modeled and discretized with 625 elements. Arc-length control is adopted. Herein, the behaviour of the element undergoing loading and unloading condi-

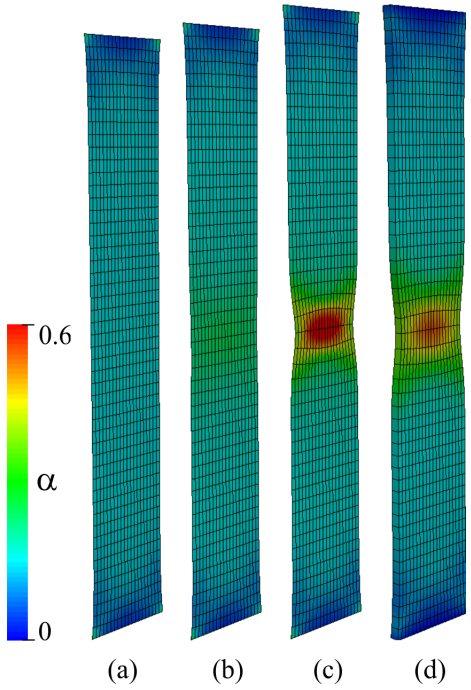

Figure 6: Plane stress necking problem. Flat tensile specimen. Hardening variable at various loading stages on the deformed configuration. (a-c) Obtained with KL shell elements at U_{norm} = 4.4, 5, 6 mm and (d) obtained with solid elements at at U_{norm} = 6 mm.

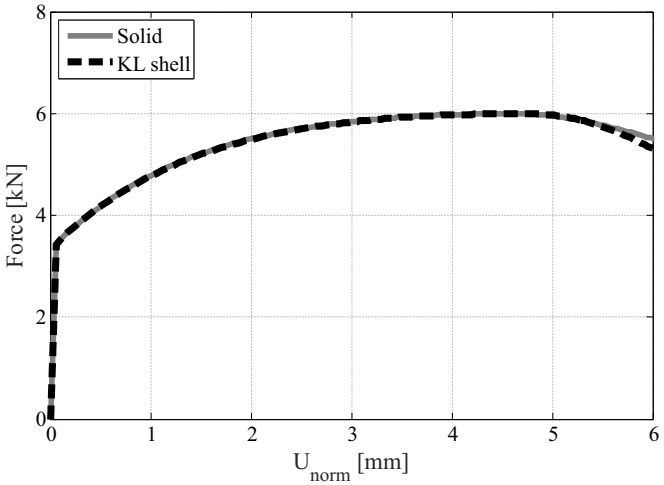

Figure 7: Plane stress necking problem. Flat tensile specimen. Load-displacement curves. Comparison between KL shell and solid elements.

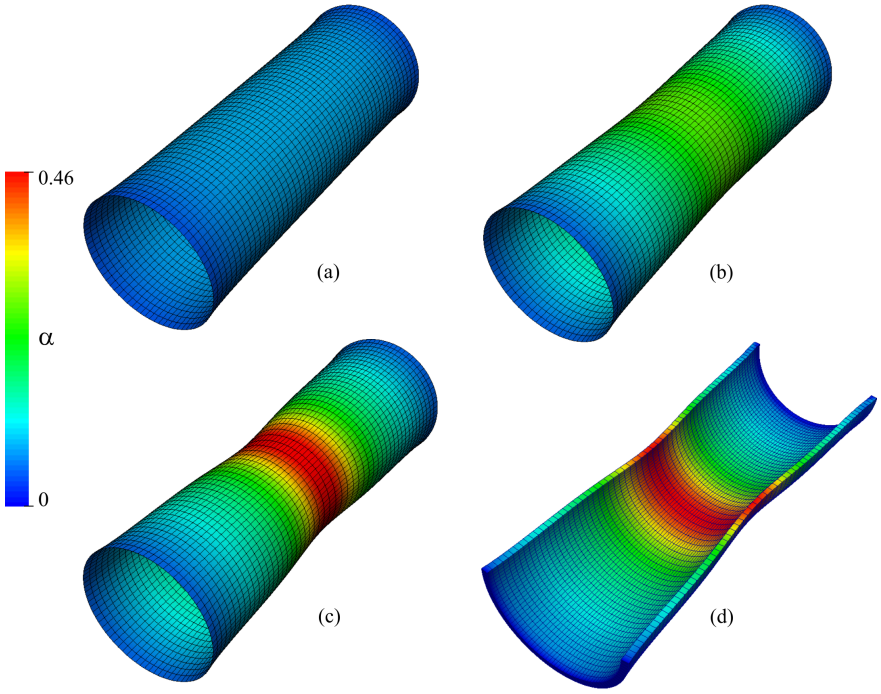

Figure 8: Plane stress necking problem. Hollow cylinder. Hardening variable at various loading stages on the deformed configuration. (a-c) Obtained with KL shell elements at U_{norm} = 2.5, 5.5, 7 mm and (d) obtained with solid elements at at U_{norm} = 7 mm (only lower half of the specimen is shown).

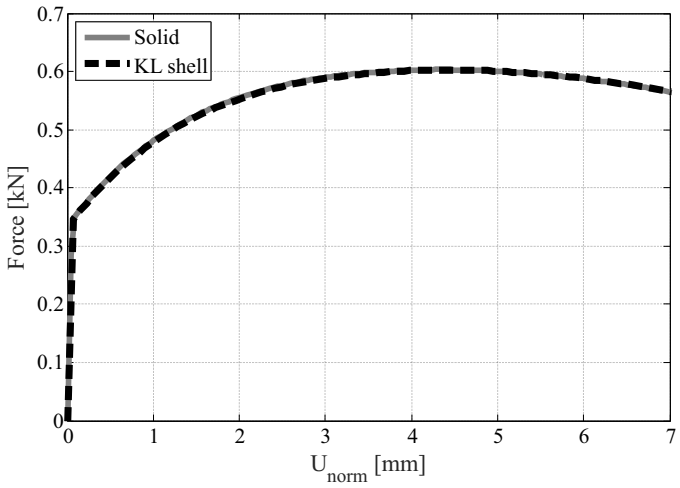

Figure 9: Plane stress necking problem. Hollow cylinder. Load-displacement curves. Comparison between KL shell and solid elements.

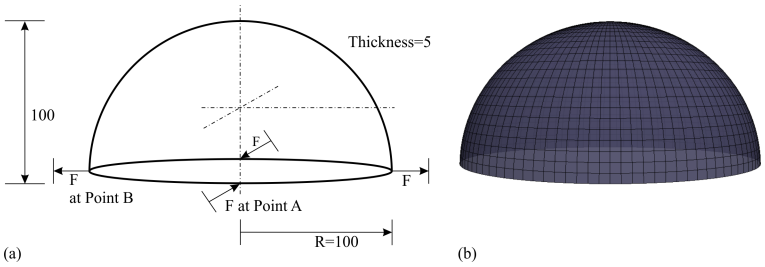

Figure 10: Pinched hemisphere at large elasto-plastic deformations. (a) Geometry and loading conditions (b) FE mesh. Dimensions in mm.

tions is investigated.

Figure 11 illustrates the hardening variable at several loading and unloading stages on the deformed configuration. The corresponding load-displacement curve is presented in Figure 12 along with results taken from [47] (which are obtained with multi-layer shell kinematics based on a six-parametric shell theory combined with finite strain plasticity). Once again, a very good agreement with the reference results can be observed.

4.4 Scordelis-Lo roof at large elasto-plastic deformations

We now examine the collapse of the Scordelis-Lo roof subjected to uniform gravity load, a classical benchmark problem for non-linear shell analysis with both geometric and material non-linearity, see e.g [6, 8, 10]. The geometry and boundary conditions of the problem are illustrated in Figure 13. The material parameters are $E = 2.1 \times 10^4$ N/mm^2, $\nu = 0$ and $R(\alpha) = 4.2$ (perfect plasticity) taken from [10]. The roof is supported by two rigid end diaphragms and is subjected to a gravity-type load with the reference self-weight value of $f0 = 4 \times 10^{-3}$ N/mm^2. Due to symmetry, only one quarter of the roof with a mesh of 1024 elements is used in the analysis. The simulation is performed under arc-length control. The reference solution is given for the vertical displacement at the midpoint of the side edge denoted as point A [10].

The evolution of the hardening variable at several loading stages on the deformed configuration is visualized in Figure 14 whereas the corresponding load-displacement curve is depicted in Figure 15 along with results taken from [10] (which are obtained with non-linear shell kinematics with large displacements and finite rotations of Reissner-Mindlin type, combined with a small-strain elasto-plasticity model). A good agreement with the reference results can be found.

4.5 Pinched cylinder at large elasto-plastic deformations

In this example, a thin cylinder bounded by two rigid diaphragms, loaded with two concentrated forces at the mid section is analyzed. It is a typical and demanding benchmark example to validate the elasto-plastic shell formulations, see e.g. [8, 10, 2, 6, 53]. The geometry and boundary conditions of the problem are shown in Figure 16. The material parameters taken from [2] are $E = 3000$,

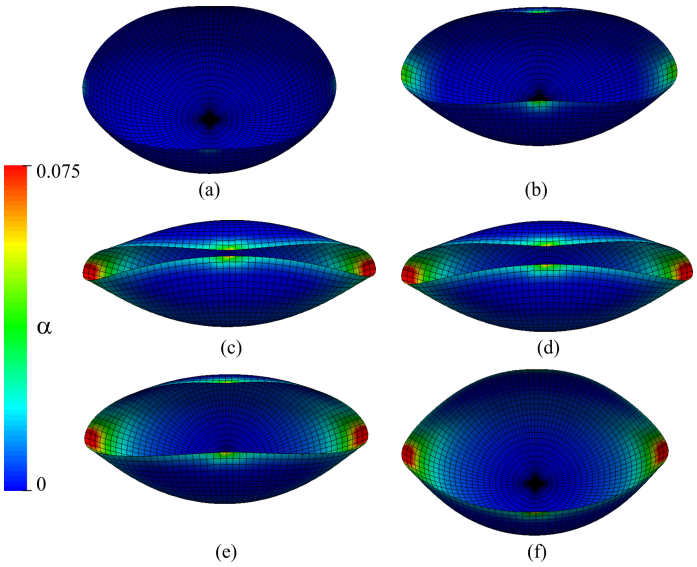

Figure 11: Pinched hemisphere at large elasto-plastic deformations. (a-f) Hardening variables at various loading and unloading stages on the deformed configuration. (a-c) Loading stages at displacement 2.54, 5.34, 9.6 x 10 mm and (d-f) unloading stages at 9.26, 6.73, 2.8 x 10 mm. The displacements correspond to point A.

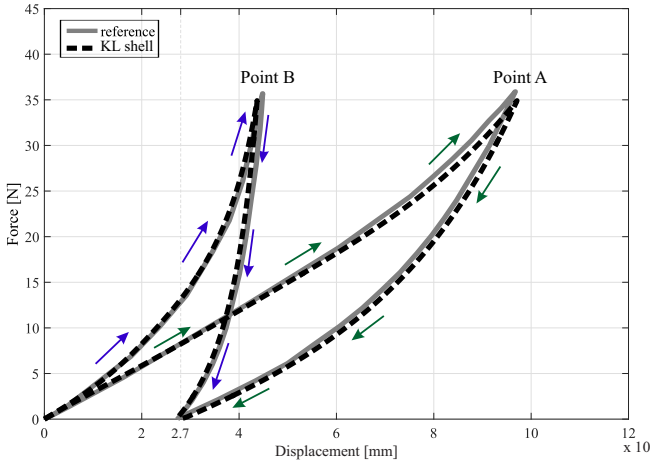

Figure 12: Pinched hemisphere at large elasto-plastic deformations. Load-displacement curves (displacements of the points of application of the load in the load direction at points A and B). Reference curve [47].

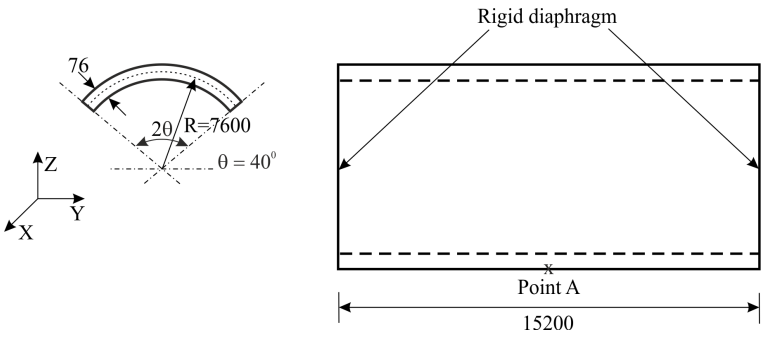

Figure 13: Collapse of Scordelis-Lo roof at large elasto-plastic deformations. Geometry. Dimensions in mm.

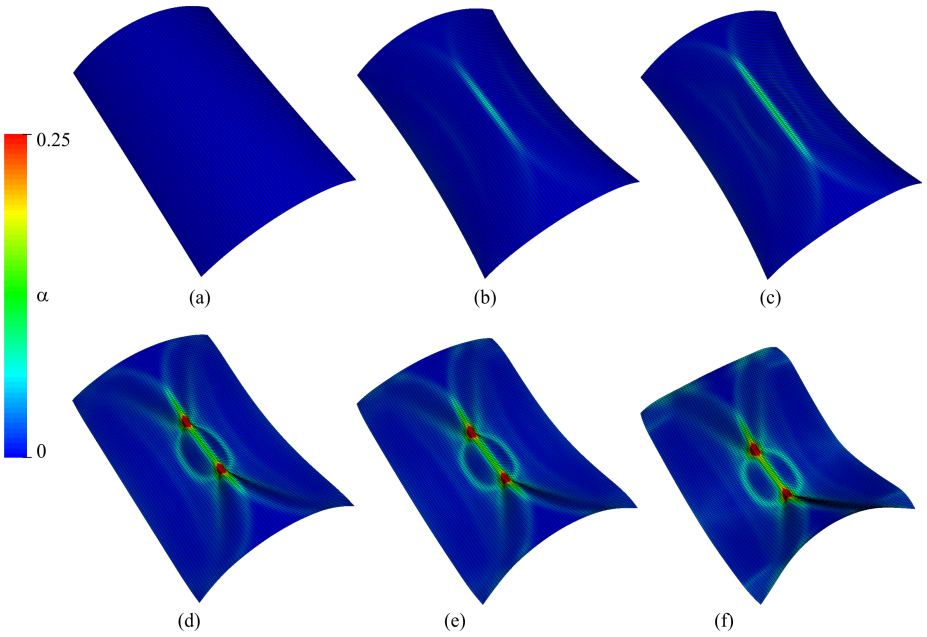

Figure 14: Collapse of Scordelis-Lo roof at large elasto-plastic deformations. (a-f) Hardening variable at various loading stages on the deformed configuration at u = 0.05, 0.75, 1.0, 1.25, 1.5, 2.5 x 1000 mm. The displacements correspond to point A.

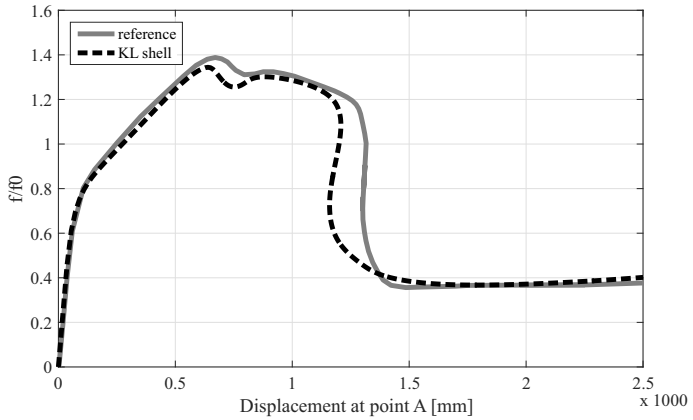

Figure 15: Collapse of Scordelis-Lo roof at large elasto-plastic deformations. Load-displacement curves. Reference curve [10].

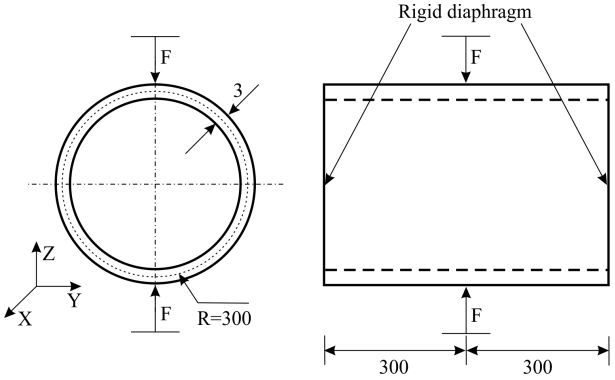

Figure 16: Pinched cylinder at large elasto-plastic deformations. Geometry and boundary conditions.

$\nu = 0.3$ and linear hardening law $R(\alpha) = 24.3 + 300\alpha$. Note that the units of geometric dimensions and material parameters are consistent. Due to symmetry, only one quarter of the shell is modeled and the spatial discretization is performed with 1024 elements. Arc-length control is adopted.

Figure 17 reports the evolution of the hardening variable at various loading stages on the deformed configurations. As can be observed, the structure undergoes large displacements, severe relative rotations, large strain warping and buckling during the loading process. The corresponding load-deflection curves are given in Figure 18 along with the results taken from [53] (which are obtained from the mixed displacement-shear strain KL shell element coupled with finite strain plasticity), and again, good agreement of the proposed formulation with the reference solution can be observed.

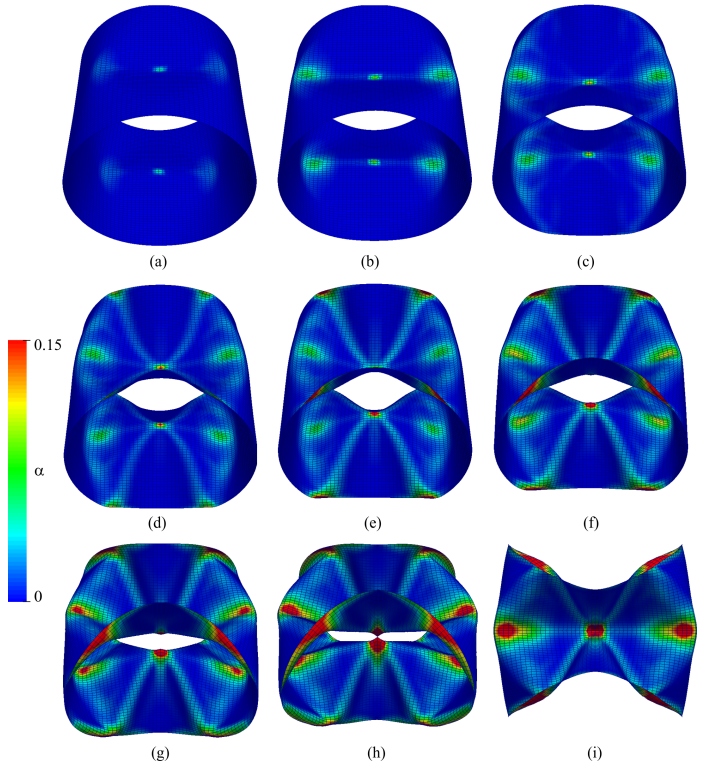

Figure 17: Pinched cylinder at large elasto-plastic deformations. (a-i) Hardening variable at various loading stages on the deformed configuration at u = 59.85, 102.19, 132.75, 165.65, 199.27, 229.98, 262.73, 299. (i) Top view at u = 299.

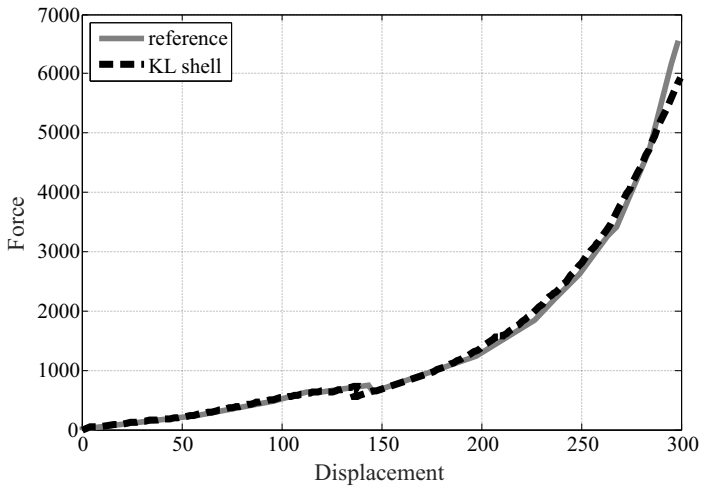

Figure 18: Pinched cylinder at large elasto-plastic deformations. Load-displacement curves. Reference curve [53].

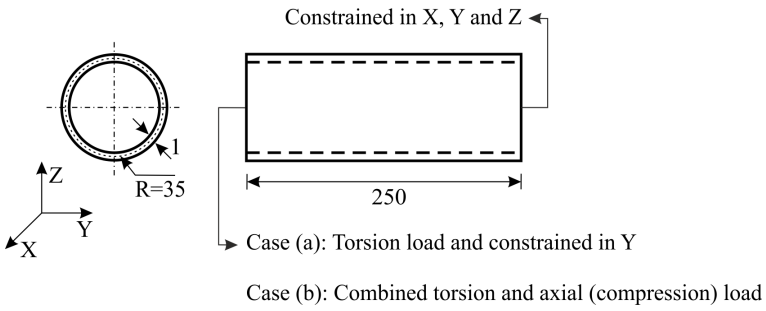

Figure 19: Twisted cylinder at large elasto-plastic deformations. Geometry and loading conditions. Dimensions in mm.

4.6 Twisted cylinder at large elasto-plastic deformations

Finally, we simulate twisting of a cylinder with the boundary and loading conditions as illustrated in Figure 19. We consider two cases, (a) torsion load and (b) combined torsion and axial load. The material parameters are the same as in example 4.2. In both the cases, the structure is discretized with 4000 elements. The calculation is performed with displacement control. For both cases, in the simulation, a geometric imperfection is introduced in center in a similar way as suggested in [20].

For both cases, a series of snapshots with the hardening variable plotted on the deformed configuration at several loading stages are shown in Figure 20 (a-f). The curves in figure 21 plot the angle of twist against the norm of the total displacement, where an applied axial displacement is given on the right vertical axis for case (b). Note that the applied loads are chosen such that no self-contact occurs.

5 Conclusions

We have presented an isogeometric thin shell formulation for large-strain elasto-plastic analysis. It is based on a stress-based approach, where the constitutive equations are evaluated at different integration points through the thickness. It is important to note that the thickness integration does not imply discretization through the thickness. Instead, only the shell midsurface is discretized. Since Kirchhoff-Love kinematics is assumed, the formulation is also rotation-free, such that the discrete formulation has only three degrees of freedom per node, namely the x, y, z displacement of the midsurface, resulting in a very efficient element formulation. Due to the chosen stress-based approach, general 3D solid constitutive models can be employed. In this paper, we employed classical J_2 plasticity with isotropic hardening, but other models could be readily used. Within such a stress-based approach, care has to be taken that the plane stress condition is not violated. This is obtained by iteratively updating the thickness stretch, which is done at the integration points. We have performed several numerical examples and compared the results with available reference results from literature and with those obtained from fully 3D solid computations. These tests confirm the accuracy, stability, and efficiency of the

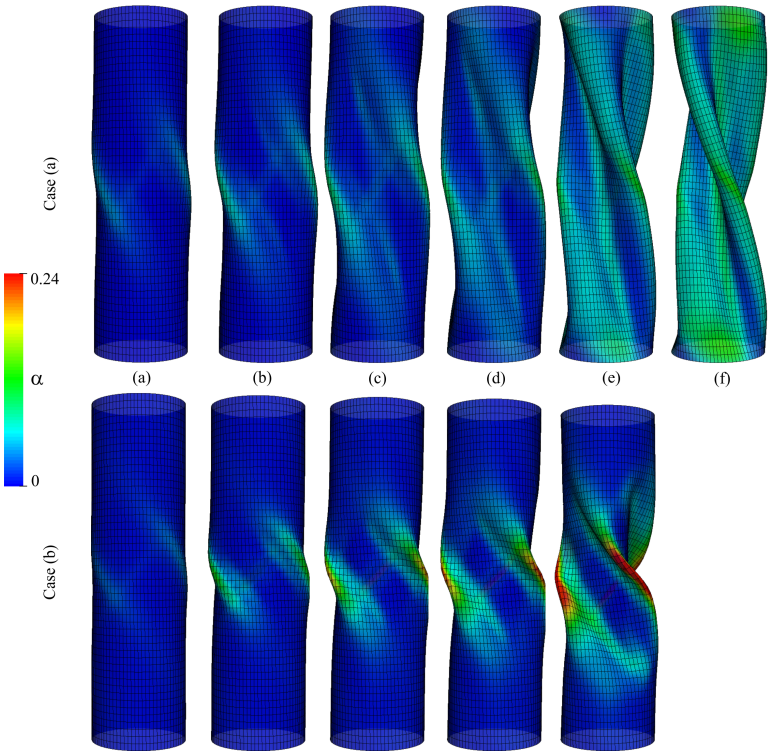

Figure 20: Twisted cylinder at large elasto-plastic deformations. (a-e) Hardening variable at various loading stages on the deformed configuration at twist angle of 5, 10, 20, 30, 66.25 degrees. (f) Final stage at twist angle of 108.25 degrees.

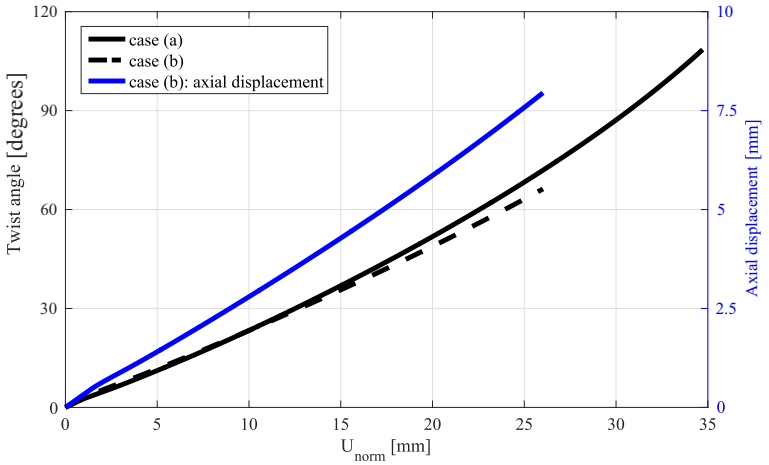

Figure 21: Twisted cylinder at large elasto-plastic deformations. Angle of twist-displacement curves.

proposed method.

Acknowledgment. This research was partially funded by the European Research Council, ERC Starting Researcher Grant INTERFACES, Grant Agreement Nr. 279439. J. Kiendl was partially funded by the Onsager fellowship program of NTNU. This support is gratefully acknowledged.

Appendix A. Time integration of elasto-plastic constitutive equations at finite strains

Solution of the elasto-plastic constitutive eqs. (11) and (12) requires a time integration scheme, which is outlined as follows. The evolution equations (flow rule and hardening law) can be integrated with the backward Euler scheme, obtaining

$$\begin{aligned} \boldsymbol{C}_{n+1}^{\mathrm{p}^{-1}} &= \boldsymbol{C}_{n}^{\mathrm{p}^{-1}} - \frac{2}{3}\Delta\lambda \mathrm{tr}[\boldsymbol{b}_{n+1}^{\mathrm{e}}]\boldsymbol{F}_{n+1}^{-1}\boldsymbol{n}_{n+1}\boldsymbol{F}_{n+1}^{-T}\,, \\ \alpha_{n+1} &= \alpha_n + \sqrt{\frac{2}{3}}\Delta\lambda\,, \end{aligned} \tag{40}$$

with $\boldsymbol{n}_{n+1} = \frac{\boldsymbol{\tau}_{\mathrm{dev},n+1}}{\|\boldsymbol{\tau}_{\mathrm{dev},n+1}\|}$ and $\Delta\lambda > 0$ as the incremental plastic multiplier. The subscripts $(\cdot)_n$ and $(\cdot)_{n+1}$ define the values of $(\cdot)$ at t_n and t_{n+1}, respectively. The Kuhn-Tucker conditions must be enforced at all times and at t_{n+1} they read

$$\begin{aligned} &f(\boldsymbol{\tau}_{\mathrm{dev},n+1}, \alpha_{n+1}) = \|\boldsymbol{\tau}_{\mathrm{dev},n+1}\| - \sqrt{\frac{2}{3}}R(\alpha_{n+1}) \leq 0\,, \\ &\Delta\lambda \geq 0, \quad f(\boldsymbol{\tau}_{\mathrm{dev},n+1}, \alpha_{n+1}) \leq 0, \quad \Delta\lambda f(\boldsymbol{\tau}_{\mathrm{dev},n+1}, \alpha_{n+1}) = 0\,. \end{aligned} \tag{41}$$

In order to solve (40) while satisfying (41), the classical elastic predictor and plastic corrector (return-mapping) algorithm outlined in [33, 34] is adopted, which is summarized in Table 1.

Elastic predictor: Given $\boldsymbol{F}_n$, $\boldsymbol{C}_n^{\mathrm{p}^{-1}}$ and α_n at t_n and $\Delta\boldsymbol{F}$

(1) Compute trial elastic stress:

$$\underline{\boldsymbol{F}}_{n+1} = J_{n+1}^{-1/3}\boldsymbol{F}_{n+1} \quad J_{n+1} = \det[\boldsymbol{F}_{n+1}] \quad \underline{\boldsymbol{b}}_{n+1}^{\mathrm{e,tr}} = \underline{\boldsymbol{F}}_{n+1}\boldsymbol{C}_n^{\mathrm{p}-1}\underline{\boldsymbol{F}}_{n+1}^{\mathrm{T}}$$

$$\boldsymbol{\tau}_{\mathrm{dev},n+1}^{\mathrm{tr}} = \mu\ \mathrm{dev}[\underline{\boldsymbol{b}}_{n+1}^{\mathrm{e,tr}}] \quad \boldsymbol{\tau}_{\mathrm{vol},n+1}^{\mathrm{tr}} = \tfrac{\kappa}{2}\left(J_{n+1}^2 - 1\right)\mathbf{I}$$

(2) Check plastic admissibility:

If $f_{n+1}^{\mathrm{tr}} = \left\|\boldsymbol{\tau}_{\mathrm{dev},n+1}^{\mathrm{tr}}\right\| - \sqrt{\tfrac{2}{3}}R(\alpha_n) \leq 0$

then (elastic process) set $(\cdot)_{n+1} = (\cdot)_{n+1}^{\mathrm{tr}}$ and exit

else (plastic process) go to (3)

(3) Plastic corrector (Return mapping):

Solve the nonlinear scalar equation for $\Delta\lambda > 0$

$$f_{n+1}^{\mathrm{tr}} = \left\|\boldsymbol{\tau}_{\mathrm{dev},n+1}^{\mathrm{tr}}\right\| - \sqrt{\tfrac{2}{3}}R(\alpha_n + \sqrt{\tfrac{2}{3}}\Delta\lambda) - \tfrac{2}{3}\Delta\lambda\mu\mathrm{tr}[\underline{\boldsymbol{b}}_{n+1}^{\mathrm{e,tr}}] = 0$$

Update the state variables

$$\boldsymbol{\tau}_{\mathrm{dev},n+1} = \boldsymbol{\tau}_{\mathrm{dev},n+1}^{\mathrm{tr}} - \tfrac{2}{3}\Delta\lambda\mu\mathrm{tr}[\underline{\boldsymbol{b}}_{n+1}^{\mathrm{e,tr}}]\boldsymbol{n}_{n+1}^{\mathrm{tr}} \quad \boldsymbol{\tau}_{\mathrm{vol},n+1} = \boldsymbol{\tau}_{\mathrm{vol},n+1}^{\mathrm{tr}}$$

$$\boldsymbol{\sigma}_{n+1} = \tfrac{1}{J}\left\{\boldsymbol{\tau}_{\mathrm{vol},n+1} + \boldsymbol{\tau}_{\mathrm{dev},n+1}\right\} \quad \boldsymbol{n}_{n+1}^{\mathrm{tr}} = \frac{\boldsymbol{\tau}_{\mathrm{dev},n+1}^{\mathrm{tr}}}{\left\|\boldsymbol{\tau}_{\mathrm{dev},n+1}^{\mathrm{tr}}\right\|}$$

$$\boldsymbol{C}_{n+1}^{\mathrm{p}^{-1}} = \boldsymbol{C}_n^{\mathrm{p}^{-1}} - \tfrac{2}{3}\Delta\lambda\mathrm{tr}[\boldsymbol{b}_{n+1}^{\mathrm{e,tr}}]\boldsymbol{F}_{n+1}^{-1}\boldsymbol{n}_{n+1}^{\mathrm{tr}}\boldsymbol{F}_{n+1}^{-T}$$

$$\alpha_{n+1} = \alpha_n + \sqrt{\tfrac{2}{3}}\Delta\lambda$$

$$\boldsymbol{S}_{n+1} = J_{n+1}\boldsymbol{F}_{n+1}^{-1}\boldsymbol{\sigma}_{n+1}\boldsymbol{F}_{n+1}^{-\mathrm{T}}$$

Compute the consistent elastoplastic tangent moduli: Table 2

Table 1: J_2-plasticity at finite strains. Elastic predictor/return-mapping algorithm [30, 33, 34].

- Scaling factors:

$$f_1 = 1 + \frac{R^{'}}{3\bar{\mu}} \quad f_2 = \left[1 - \frac{1}{f_1}\right] \frac{2}{3} \frac{\left\|\boldsymbol{\tau}^{\mathrm{tr}}_{\mathrm{dev},n+1}\right\|}{\bar{\mu}} \Delta\lambda \quad \boldsymbol{n} = \boldsymbol{n}^{\mathrm{tr}}_{n+1} \quad \bar{\mu} = \frac{1}{3}\mu \mathrm{tr}(\underline{\boldsymbol{b}}^{\mathrm{e}})$$

$$\delta_1 = \frac{2\bar{\mu}\Delta\lambda}{\left\|\boldsymbol{\tau}^{\mathrm{tr}}_{\mathrm{dev},n+1}\right\|} \quad \delta_2 = \frac{1}{f_1} - \delta_1 + f_2 \quad \delta_3 = \left[\frac{1}{f_1} - \delta_1\right] \frac{\left\|\boldsymbol{\tau}^{\mathrm{tr}}_{\mathrm{dev},n+1}\right\|}{\bar{\mu}}$$

- Spatial elasticity tensor $\mathfrak{c}^{\mathrm{e,tr}}_{n+1}$:

$$\mathfrak{c}^{\mathrm{e,tr}}_{n+1} = \frac{1}{J}\left[\mathfrak{c}^{\mathrm{e,tr}}_{\mathrm{vol},n+1} + \mathfrak{c}^{\mathrm{e,tr}}_{\mathrm{dev},n+1}\right]$$

$$\mathfrak{c}^{\mathrm{e,tr}}_{\mathrm{vol},n+1} = \kappa_0\left[J^2\mathbf{I}\otimes\mathbf{I} - (J^2-1)\mathbf{II}\right]$$

$$\mathfrak{c}^{\mathrm{e,tr}}_{\mathrm{dev},n+1} = 2\bar{\mu}\mathbf{II}_{\mathrm{d}} - \frac{2}{3}\left[(\boldsymbol{\tau}^{\mathrm{tr}}_{\mathrm{dev},n+1}\otimes\mathbf{I}) + (\mathbf{I}\otimes\boldsymbol{\tau}^{\mathrm{tr}}_{\mathrm{dev},n+1})\right]$$

- Spatial consistent tangent moduli $\mathfrak{c}_{n+1}$:

$$\mathfrak{c}_{n+1} = \frac{1}{J}\left[\mathfrak{c}^{\mathrm{e,tr}}_{\mathrm{vol},n+1} + \mathfrak{c}^{\mathrm{e,tr}}_{\mathrm{dev},n+1}(1-\delta_1) - 2\bar{\mu}\delta_2\boldsymbol{n}\otimes\boldsymbol{n} - 2\bar{\mu}\delta_3\boldsymbol{n}\otimes\mathrm{dev}[\boldsymbol{n}^2]\right]$$

- Material consistent tangent moduli $\mathbb{C}$:

$$\mathbb{C} = J\boldsymbol{F}^{-1}\boldsymbol{F}^{-1}\mathfrak{c}\,\boldsymbol{F}^{-1}\boldsymbol{F}^{-1}$$

Table 2: J_2-plasticity at finite strains. Consistent elasto-plastic tangent moduli for the return mapping algorithm [30, 34] where $\mathbf{II}$ is the fourth-order symmetric identity tensor and $\mathbf{II}_{\mathrm{d}}$ is the deviatoric projection tensor defined as $\mathbf{II}_{\mathrm{d}} = \mathbf{II} - \frac{1}{3}\mathbf{I}\otimes\mathbf{I}$.

References

[1] Crisfield MA, Peng X (1992) Efficient nonlinear shell formulations with large rotations and plasticity, in: D.R.J. Owen et al. (Eds.), Computational Plasticity: Models, Software and Applications, Part 1, Pineridge Press, Swansea 1979–1997

[2] Simo JC and Kennedy JG (1992) On a stress resultant geometrically exact shell model. Part V. Nonlinear plasticity: formulation and integration algorithms. Computer Methods in Applied Mechanics and Engineering 96: 133–171

[3] Skallerud B, Haugen B (1999) Collapse of thin shell structures - stress resultant plasticity modelling with a co-rotated ADNES finite element formulation. International Journal for Numerical Methods in Engineering 46:1961–1986

[4] Skallerud B, Myklebust LI, Haugen B (2001) Nonlinear response of shell structures: effects of plasticity modelling and large rotations. Thin-Walled Structures 39: 463–482

[5] Zeng Q, Combescure A, Arnaudeau F (2001) An efficient plasticity algorithm for shell elements application to metal forming simulation. Computers & Structures 79: 1525–1540

[6] Dujc J, Brank B (2012) Stress resultant plasticity for shells revisited. Computer Methods in Applied Mechanics and Engineering 247–248:146–165

[7] Wagner W, Gruttmann F (2005) A robust non-linear mixed hybrid quadrilateral shell element. International Journal for Numerical Methods in Engineering 64:635–666

[8] Kim KD, Lomboy GR (2006) A co-rotational quasi-conforming 4-node resultant shell element for large deformation elasto-plastic analysis. Computer Methods in Applied Mechanics and Engineering 195:6502–6522

[9] Dal Cortivo N, Felippa CA, Bavestrello H, Silva WTM (2009) Plastic buckling and collapse of thin shell structures, using layered plastic modeling and corotational ANDES finite elements. Computer Methods in Applied Mechanics and Engineering 198:785–798

[10] Brank B, Perić D, Damjanić FB (1997) On large deformation of thin elastoplastic shells: implementation of a finite rotation model for quadrilateral shell elements. International Journal for Numerical Methods in Engineering 40:689–726

[11] Klinkel S, Govindjee S (2002) Using finite strain 3D-material models in beam and shell elements. Engineering Computations 19(3):254–271

[12] Bischoff M, Wall WA, Bletzinger KU, and Ramm E (2004) Models and finite elements for thin-walled structures. In E. Stein, R. de Borst, and T.J.R. Hughes, editors, Encyclopedia of Computational Mechanics, volume 2, Solids, Structures and Coupled Problems, chapter 3. Wiley

[13] Hughes TJR, Cottrell JA, Bazilevs Y (2005) Isogeometric analysis: CAD, finite elements, NURBS, exact geometry and mesh refinement. Computer Methods in Applied Mechanics and Engineering. 194:4135–4195

[14] Kiendl J, Bletzinger KU, Linhard J, Wüchner R (2009) Isogeometric shell analysis with Kirchhoff-Love elements. Computer Methods in Applied Mechanics and Engineering 198:3902–3914

[15] Kiendl J, Hsu MC, Wu MCH, Reali A (2015) Isogeometric Kirchhoff-Love shell formulations for general hyperelastic materials. Computer Methods in Applied Mechanics and Engineering 291:280–303

[16] Kiendl J (2011) Isogeometric analysis and shape optimal design of shell structures. PhD dissertation, Technische Universtität München

[17] Nguyen-Thanh N, Kiendl J, Nguyen-Xuan H, Wüchner R, Bletzinger KU, Bazilevs Y, Rabczuk T (2011) Rotation free isogeometric thin shell analysis using PHT-splines. Computer Methods in Applied Mechanics and Engineering 200(47–48): 3410–3424

[18] Benson DJ, Bazilevs Y, Hsu MC, Hughes TJR (2011) A large deformation, rotation-free, isogeometric shell. Computer Methods in Applied Mechanics and Engineering 200: 1367–1378

[19] Duong TX, Roohbakhshan F, Sauer RA (2017) A new rotation-free isogeometric thin shell formulation and a corresponding continuity constraint for patch boundaries. Computer Methods in Applied Mechanics and Engineering 316: 43–83

[20] Benson DJ, Bazilevs Y, Hsu MC, Hughes TJR (2010) Isogeometric shell analysis: The Reissner-Mindlin shell. Computer Methods in Applied Mechanics and Engineering 199:276–289

[21] Dornisch W, Klinkel S, Simeon B (2013) Isogeometric Reissner-Mindlin shell analysis with exactly calculated director vectors. Computer Methods in Applied Mechanics and Engineering 253: 491–504

[22] Dornisch W, Klinkel S (2014) Treatment of Reissner-Mindlin shells with kinks without the need for drilling rotation stabilization in an isogeometric framework. Computer Methods in Applied Mechanics and Engineering 276: 35–66

[23] Dornisch W, Müller R, Klinkel S (2016) An efficient and robust rotational formulation for isogeometric Reissner-Mindlin shell elements. Computer Methods in Applied Mechanics and Engineering 303:1–34

[24] Oesterle B, Sachse R, Ramm E, Bischoff M (2017) Hierarchic isogeometric large rotation shell elements including linearized transverse shear parametrization. Computer Methods in Applied Mechanics and Engineering 321:383–405

[25] Echter R, Oesterle B, Bischoff M (2013) A hierarchic family of isogeometric shell finite elements. Computer Methods in Applied Mechanics and Engineering 254 (0):170–180

[26] Echter R (2013) Isogeometric Analysis of Shells. PhD dissertation, Universtität Stuttgart

[27] Hosseini S, Remmers JJC, Verhoosel CV, de Borst R (2013) An isogeometric solid-like shell element for nonlinear analysis, International Journal for Numerical Methods in Engineering 95:238–256

[28] Bouclier R, Elguedj T, Combescure A (2013) Efficient isogeometric NURBS-based solid-shell elements: Mixed formulation and B-bar-method. Computer Methods in Applied Mechanics and Engineering 267:86–110

[29] Caseiro JF, Valente RAF, Reali A, Kiendl J, Auricchio F, Alves de Sousa RJ (2015) Assumed Natural Strain NURBS-based solid-shell element for the analysis of large deformation elasto-plastic thin-shell structures. Computer Methods in Applied Mechanics and Engineering 284:861–880

[30] Simo, JC, Hughes TJR (1998) Computational Inelasticity. Springer-Verlag, New York.

[31] Neto EdS, Perić D, Owen DRJ (2008) Computational methods for plasticity. John Wiley & Sons Ltd, 2008

[32] Basar Y and Krätzig W (1985) Mechanik der Flächentragwerke. Vieweg, Braunschweig

[33] Simo JC (1998) A framework for finite strain elastoplasticity based on maximum plastic dissipation and the multiplicative decomposition. Part I: continuum formulation. Computer Methods in Applied Mechanics and Engineering 66:199–219

[34] Simo JC (1988) A framework for finite strain elastoplasticity based on maximum plastic dissipation and the multiplicative decomposition. Part II: computational aspects. Computer Methods in Applied Mechanics and Engineering 68:1–31

[35] Xiao H, Bruhns OT, Meyers A (2006) Elastoplasticity beyond small deformations. Acta Mechanica 182:31–111

[36] Naghdi PM (1990) A critical review of the state of finite plasticity. Journal of Applied Mathematics and Physics 41:315–394

[37] Holzapfel GA (2000) Nonlinear solid mechanics: A continuum approach for engineering. Wiley, 1st edition

[38] Bonet J and Wood DW (2008) Nonlinear continuum mechanics for finite element analysis. Cambridge University Press, 2nd edition.

[39] Dodds Jr. RH (1987) Numerical Techniques for Plasticity Computations in Finite Element Analysis. Computers and Structures 26(5):767–779

[40] Belytschko T, Liu WK, Moran B (2000) Nonlinear Finite Elements for Continua and Structures. Wiley

[41] Corradi Dell'Acqua L (2010) Meccanica delle Strutture 3 Volume: La valutazione della capacità portante, McGraw-Hill (Milano)

[42] Mühlhaus HB, Aifantis EC (1991) A variational principle for gradient plasticity. International Journal of Solids and Structures 28:845–857.

[43] Geers MGD (2004) Finite strain logarithmic hyperelasto-plasticity with softening: a strongly non-local imlicit gradient framework. Computer Methods in Applied Mechanics and Engineering 193:3377–3401.

[44] Reddy B, Ebobisse F, McBride A (2008) Well-posedness of a model of strain gradient plasticity for plastically irrotational materials. International Journal of Plasticity 24:55–73.

[45] Miehe C (2011) A multi-field incremental variational framework for gradient-extended standard dissipative solids. Journal of the Mechanics and Physics of Solids 59:898–923.

[46] Ambati M, Kruse R, De Lorenzis L (2016) A phase-field model for ductile fracture at finite strains and its experimental verification. Computational Mechanics 57:149–167

[47] Başar Y, Itskov M (1998) Finite element formulation of the Ogden material model with application to rubber-like shells. International Journal for Numerical Methods in Engineering 42:1279–1305

[48] Wagner W, Klinkel S, Gruttmann F (2002) Elastic and plastic analysis of thinwalled structures using improved hexahedral elements. Computers and Structures 80: 857–869

[49] Klinkel S, Gruttmann F, Wagner W (2006) A robust non-linear solid shell element based on a mixed variational formulation. Computer Methods in Applied Mechanics and Engineering 195(1-3):179–201

[50] Klinkel S, Gruttmann F, Wagner W (2008) A mixed shell formulation accounting for thickness strains and finite strain 3d material models. International Journal for Numerical Methods in Engineering 74:945–970

[51] Başar Y, Itskov M (1999) Constitutive model and finite element formulation for large strain elasto-plastic analysis of shells. Computational Mechanics 23:466–481

[52] Eberlein R, Wriggers P (1999) Finite element concepts for finite elastoplastic strains and isotropic stress response in shells: theoretical and computational analysis. Computer Methods in Applied Mechanics and Engineering 171(3-4):243–279

[53] Areias PMA, Ritto-Corrêa MC, Martins (2010) Finite strain plasticity, the stress condition and a complete shell model. Computational Mechanics 45:189–209